ENG. Struct. Civ. Eng. 2026, 20(4): 690–705
https://doi.org/10.1007/s11709-026-1295-7

RESEARCH ARTICLE

Physics-Informed Machine Learning framework enhancing predictive accuracy and interpretability of fiber-reinforced polymer-confined concrete cylinders

Wenyu WANG[a], Kui HU[a*], Xiaotong DU[a], Syed Tafheem Abbas GILLANI[a], Giuseppe Carlo MARANO[a,b]

[a] *School of Civil Engineering, Henan University of Technology, Zhengzhou 450001, China*
[b] *Department of Structural, Geotechnical and Building Engineering, Politecnico di Torino, Turin 10129, Italy*
[*] *Corresponding author. E-mail: mailhukui@haut.edu.cn*

ABSTRACT Empirical models for Fiber-Reinforced Polymer (FRP)-confined concrete cylinders often show limited accuracy due to complex confinement behavior and small-sample constraints. This study develops a Physics-Informed Machine Learning (PIML) framework that embeds axial constitutive equations into ensemble learning models to enhance prediction accuracy and interpretability. Physical stress–strain laws are integrated into extreme gradient boosting and random forest loss functions through Lagrangian multipliers, while Bayesian optimization with *K*-fold validation improves model generalization. Using 310 experimental data sets, the optimized PIML model achieved a 47.7% lower root mean square error and 32% less uncertainty compared with eight empirical formulations, maintaining below 10% error for 85% of test cases. Feature analysis identified $\varepsilon_{h,rup}$, s_f, and f_l as dominant parameters consistent with FRP confinement mechanisms. The proposed PIML framework effectively bridges data-driven learning and physical theory, offering a robust and interpretable approach for intelligent design and robotic construction of FRP-confined concrete structures.

KEYWORDS Physics-Informed Machine Learning, fiber-reinforced polymer-confined concrete, Bayesian optimization, ensemble learning, predictive interpretability

1 Introduction

Structural columns serve as the fundamental load-bearing and stabilizing components of modern buildings, directly influencing overall safety and urban resilience [1]. In high-rise construction, columns must sustain large axial loads and remain functional under seismic events exceeding magnitude 8 [2], while industrial infrastructures are required to resist decades of mechanical fatigue and corrosion with reliability above 99% [3]. Such stringent performance demands underscore the growing complexity of structural design and expose the limitations of conventional strengthening approaches [4]. Accordingly, developing reliable and interpretable models to predict and optimize the behavior of structural columns under various confinement conditions has become essential for enhancing structural performance and mitigating disaster-induced losses.

Among various retrofitting and strengthening techniques, Fiber-Reinforced Polymer (FRP) confinement has emerged as a promising solution due to its high strength-to-weight ratio, corrosion resistance, and ease of application [5]. Partial confinement configurations, in particular, enable targeted reinforcement of critical zones while minimizing material consumption [6]. However, their effectiveness depends strongly on the complex interaction between confined and unconfined regions, leading to pronounced heterogeneity in stress–strain responses [7]. This complexity limits the predictive accuracy of existing empirical and semi-empirical models. Consequently, establishing a high-fidelity and interpretable framework to accurately predict the strength and strain capacity of partially FRP-confined concrete cylinders has become a critical challenge for ensuring

Article history: Received Oct 8, 2025; Accepted Dec 1, 2025

both structural safety and cost efficiency.

Early modeling efforts for FRP-confined concrete primarily relied on empirical and semi-empirical formulations derived from regression analyses of limited experimental data [8]. These equations provided acceptable predictions under ideal full-confinement conditions [9] but showed pronounced inaccuracy when applied to partially confined systems, where the mechanical response becomes highly heterogeneous [10]. In such configurations, lateral stress distribution is nonuniform, and axial strain evolution exhibits strong nonlinear coupling between confined and unconfined zones [11]. Traditional models typically assume uniform confinement pressure—a simplification that fails to represent the localized damage progression and gradual stress transfer in partially wrapped specimens [12]. As a result, prediction errors often manifest in practice, leading to either overly conservative designs that inflate material costs or underestimated capacities that compromise safety margins [13]. This discrepancy underscores the need for advanced predictive frameworks capable of capturing the localized, nonlinear, and multiscale behavior of FRP partially confined concrete, which is crucial for enhancing design reliability and extending field applicability.

Recent advances in data-driven modeling have introduced Machine Learning (ML) as a powerful alternative to traditional empirical methods, enabling nonlinear mapping between input features and structural responses without relying on predefined constitutive assumptions [14]. Early applications demonstrated that ML algorithms, such as artificial neural networks and support vector regression, could outperform classical empirical models in predicting both axial strength and ultimate strain [15]. Subsequent developments in ensemble learning, particularly gradient boosting and Random Forest (RF) algorithms, further improved predictive stability and accuracy across heterogeneous data sets [16]. However, most existing studies treat the learning process as purely statistical, neglecting the physical mechanisms governing FRP confinement. Without integration of domain knowledge, these black-box models are prone to overfitting when trained on small or noisy data sets and often lack interpretability from an engineering mechanics perspective [17]. Hence, embedding fundamental stress–strain relationships and confinement laws into ML frameworks becomes essential for achieving both high predictive fidelity and physical transparency.

To address the inherent trade-off between model accuracy and interpretability, recent research has incorporated optimization strategies into ML frameworks. Among them, Bayesian Optimization (BO) has emerged as an efficient approach for hyperparameter tuning under data scarcity, systematically balancing exploration and exploitation within complex parameter spaces [18]. When coupled with *K*-fold cross-validation, it not only enhances model generalization and robustness but also mitigates overfitting caused by limited experimental samples [19]. In the present study, BO is employed to automatically calibrate critical hyperparameters, such as tree depth, learning rate, and ensemble size, ensuring that nonlinear interactions among mechanical parameters are precisely captured [20]. This process, combined with cross-validation, maximizes the utilization of available data and minimizes noise sensitivity, resulting in stable and accurate predictions across diverse confinement configurations [21]. Therefore, BO serves as a pivotal component in realizing the proposed Physics-Informed Machine Learning (PIML) framework, which seamlessly integrates physical constitutive theory with data-driven inference to enhance both predictive reliability and interpretability for FRP-confined concrete systems.

To overcome the above limitations, this study develops a PIML framework for predicting the axial strength and strain of FRP partially confined concrete cylinders. A database of 310 tests covering geometry, material, and confinement parameters is established. The framework embeds physical stress–strain laws into the loss functions of Extreme Gradient Boosting (XGBoost) and RF models via Lagrangian constraints, ensuring physical consistency. BO with *K*-fold validation is applied to enhance accuracy and prevent overfitting under limited data. An explicit predictive equation is further derived by coupling model-derived feature importance with classical formulations. The proposed framework effectively integrates physical theory with data-driven learning, achieving high predictive accuracy and interpretability while supporting intelligent design and robotic construction of FRP-confined structures.

2 Methodology

2.1 Random forest

RF (Fig. 1) is a bagging-based ensemble learning method that constructs multiple independent decision trees using randomly sampled subsets of the training data. During prediction, the results of all trees are averaged to produce a final output. This mechanism enhances model stability and reduces overfitting, especially when dealing with small and noisy data sets. In this study, RF is used to establish a baseline predictive model with strong generalization ability and robustness to variable uncertainty in the experimental data.

2.2 Extreme gradient boosting

XGBoost (Fig. 1) is a boosting-based ensemble algorithm

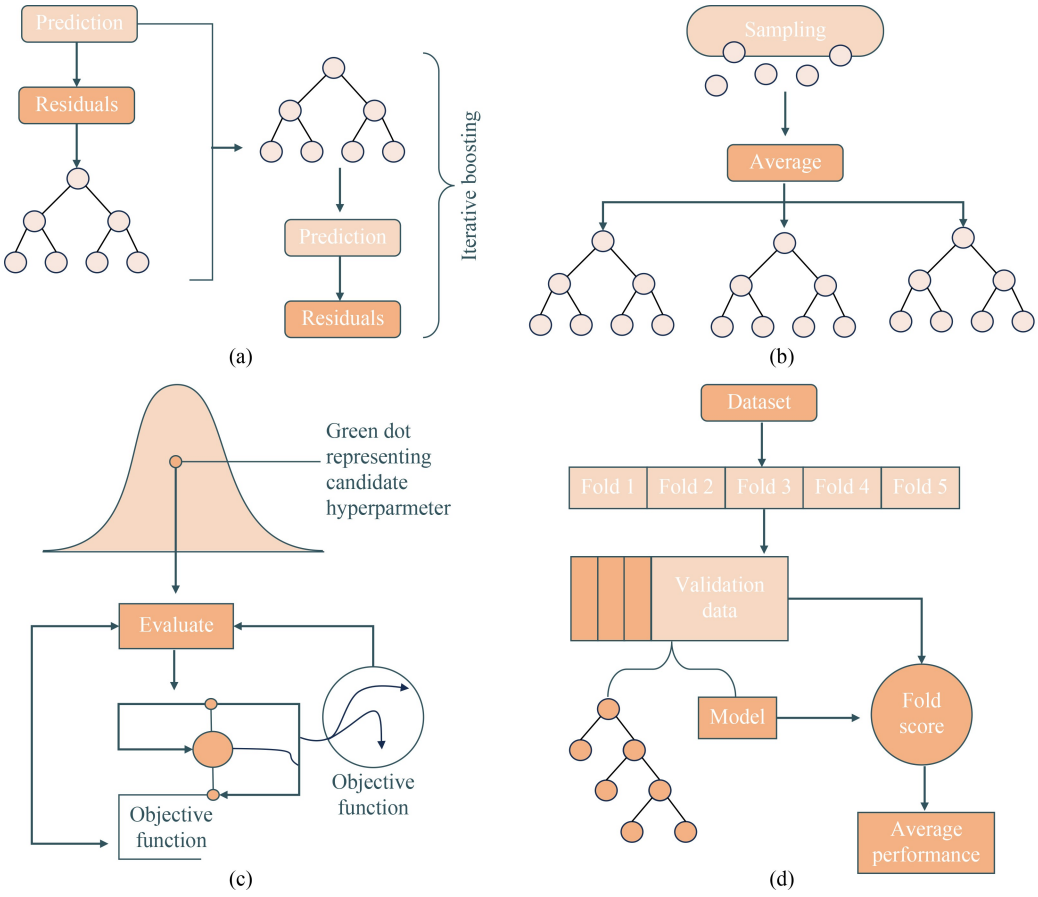

Fig. 1 ML methodology architecture: (a) RF; (b) XGBoost; (c) BO; (d) 5-fold cross-validation.

that sequentially builds decision trees to correct the errors of previous trees. Each new tree is trained to minimize a regularized objective function, which includes both the loss between predicted and true values and a penalty term that constrains model complexity. Its ability to model complex nonlinear relationships, combined with advanced regularization and parallelization techniques, makes it particularly effective in small-to-medium data sets. In this research, XGBoost is used as the core learning engine to capture intricate interactions between geometric, material, and confinement features, and to support the integration of physical constraints into the learning process.

2.3 Bayesian optimization for hyperparameter tuning

To enhance prediction accuracy and generalization under limited and noisy data, this study applies BO for hyperparameter tuning. Compared to inefficient grid or random search, BO uses a probabilistic surrogate model to efficiently explore the hyperparameter space and find near-optimal settings. BO typically uses a Gaussian Process (GP) or Tree-structured Parzen Estimator to approximate the objective function. It selects new hyperparameters by maximizing an acquisition function that balances exploration and exploitation, achieving faster convergence with fewer evaluations. In this study, BO is applied to RF and XGBoost models. Optimized hyperparameters include:

1) RF: n_estimators, max_depth, max_feature;

2) XGBoost: n_estimators, max_depth, learn_rate, gamma, reg_alpha, reg_lambda, min_child_weight, subsample, colsample_bytree.

To ensure robustness and avoid overfitting, 5-fold cross-validation (Fig. 1) is used during BO. This approach yields better model accuracy and lower variance than manual or default tuning.

2.4 Physics-informed machine learning strategy

Although data-driven ML models effectively capture nonlinear patterns, their black-box nature and lack of physical insight limit generalization and interpretability, especially with small data sets. To overcome this, a PIML approach is adopted by embedding domain knowledge, specifically, the axial stress–strain relationship of FRP-confined concrete, into model training.

PIML introduces a physical constraint into the loss function. For FRP-confined concrete, a theoretical stress–strain expression, derived from confinement mechanics and validated experimentally, is used as a residual penalty term. The modified loss function is:

$$\mathcal{L}_{\text{PIML}} = \mathcal{L}_{\text{data}} + \beta \cdot \mathcal{L}_{\text{physics}}, \quad (1)$$

where $\mathcal{L}_{\text{data}}$ is the standard data loss; $\mathcal{L}_{\text{physics}}$ measures deviation from theoretical stress–strain behavior; β is a weighting factor balancing data fit and physical consistency.

This regularization guides the model to fit the data while aligning with physical laws. In this study, the physical term is based on an empirical stress–strain expression involving confinement ratio, unconfined strength, and FRP hoop strain. PIML is implemented in XGBoost and RF by customizing their loss functions or applying post-training physics checks. This ensures the model learns both data patterns and physical behavior, improving generalization to new scenarios. The framework is illustrated in Fig. 2.

2.5 Result evaluation index algorithm

Four performance metrics were used to evaluate the ML models and the existing models, which are the root mean square error (*RMSE*), coefficient of variation (*CoV*), average value (*MEAN*), and the average absolute error (*AAE*): *RMSE* is used to indicate how much error the model will produce in predictions, with higher weights for larger errors; *CoV* is an indicator of the relative scatter of the values; *MEAN* indicates the average performance of the overall predict compared to the original data; *AAE* was used to establish the overall accuracy of the models. The four indicators are classic indicators for evaluating the prediction accuracy, which can intuitively reflect the error, discreteness, and accuracy of the prediction results, and can comprehensively evaluate each model.

$$RMSE = \sqrt{\frac{\sum_{i=1}^{n}(y_i - y_{oi})^2}{n}}, \quad (2)$$

$$MEAN = \frac{\sum_{i=1}^{n}\frac{y_i}{y_{oi}}}{n}, \quad (3)$$

$$CoV = \frac{\sqrt{\frac{\sum_{i=1}^{n}\left(\frac{y_i}{y_{oi}} - MEAN\right)^2}{n}}}{MEAN}, \quad (4)$$

$$AAE = \frac{\sum_{i=1}^{n}\left|\frac{y_i - y_{oi}}{y_{oi}}\right|}{n}, \quad (5)$$

where n refers to the number of training or testing data, i represents the ith set of input, y_i refers to the input of actual value, y_{oi} is the output for the predicted value, and $\bar{y}$ refers to the mean for the input of actual value.

3 Database

3.1 Design-oriented models

3.1.1 Unified effective confinement stress calculation

The confinement mechanism is schematically shown in Fig. 3. The lateral confined stress (f_{l1}) supplied by FRP in the case of fully wrapped confined concrete cylinders can be presumed to be evenly distributed around the circumference. The confining effect of the FRP on the core concrete is passive [12]. Stated differently, the lateral expansion of the core concrete initiates the confinement of the FRP, and as this expansion develops, the confining stress also increases until the FRP ruptures and the system fails. According to the force-balance relationship, the lateral confining stress applied to concrete by the FRP (f_{l1}) can be theoretically calculated from Eq. (7) as a function of the ultimate tensile strain

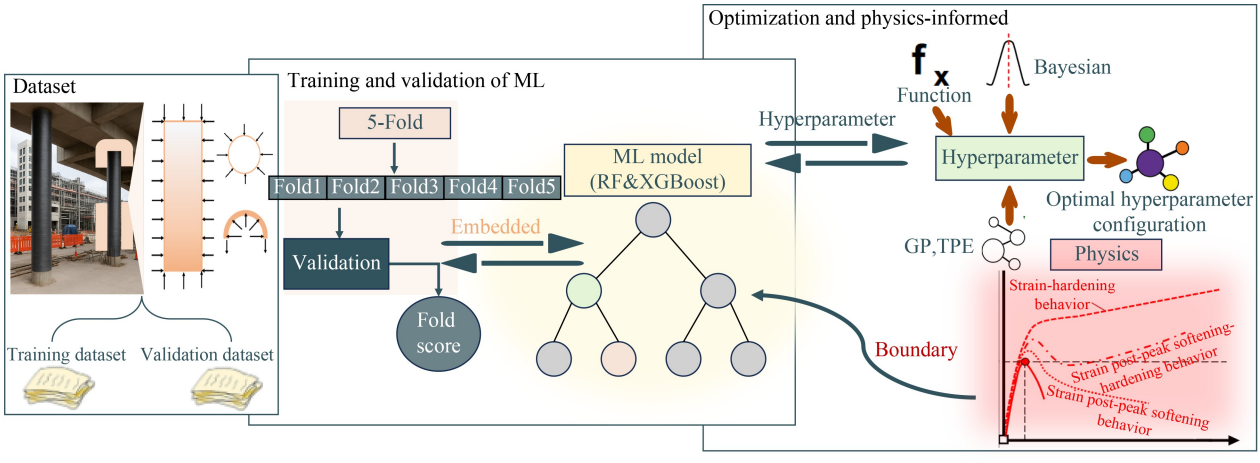

Fig. 2 The PIML framework.

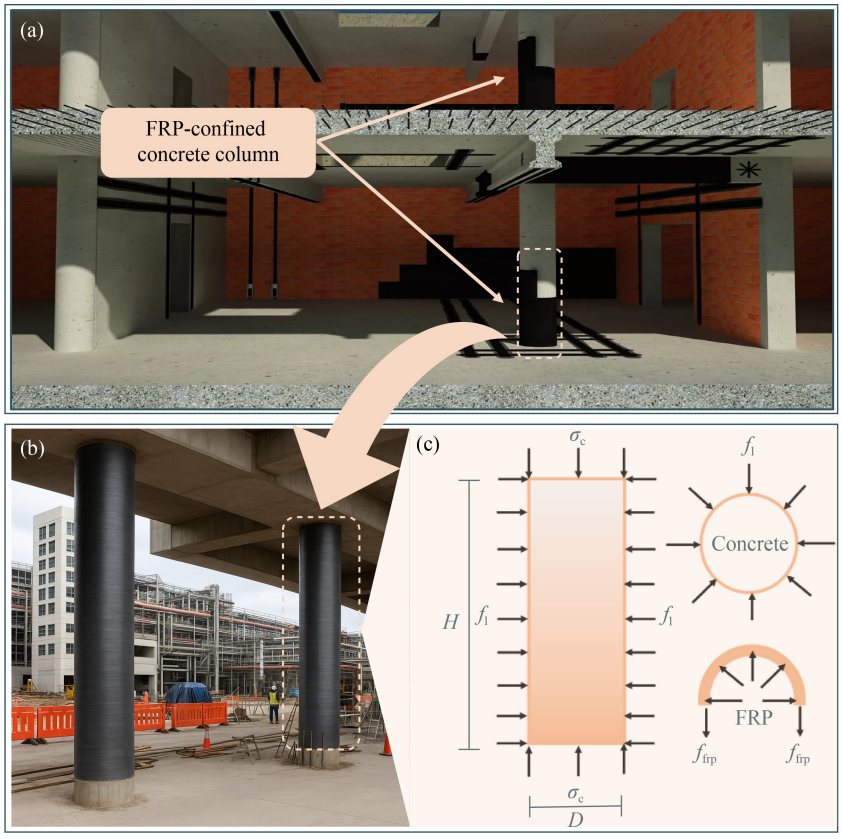

Fig. 3 (a) Conceptual diagram; (b) engineering scene diagram; (c) confinement mechanism diagram.

(ε_f) of FRP.

$$f_{l1} = \frac{2E_f t_f \varepsilon_f}{D}. \tag{6}$$

where E_f denotes the elastic modulus of FRP, t_f denotes the thickness of FRP, and D denotes the diameter of the cylinder.

In real-world applications, FRP is frequently destroyed before reaching ε_f due to the influence of technical operation, material physical qualities, and other factors. This conclusion is also drawn from the experimental results in the literature that is currently available [22,23]. To increase the accuracy of the design model, Lam and Teng [14] suggested using the actual FRP circumferential rupture strain $\varepsilon_{h,rup}$ to compute the lateral restraining pressure (f_{l1}) of FRP. Furthermore, a strain reduction factor (k_ε) was introduced by Pessiki et al. [24]. The formulas are as follows:

$$\varepsilon_{h,rup} = k_\varepsilon \varepsilon_f, \tag{7}$$

$$f_{l1} = \frac{2k_\varepsilon E_f \varepsilon_f t_f}{D}. \tag{8}$$

According to some research [25–27], the confining effect of partially FRP confined concrete is less than that of fully confining. The "arch effect" hypothesis, which uses a parabola with a starting tangent of 45° to the horizontal to discriminate between effective and ineffective constraint regions, is widely used internationally to explain this occurrence. By taking into account the local confinement impact of circumferential strips of FRP, the vertical confinement coefficient k_v, which is relevant to partial confinement, is proposed with the following equation:

$$k_v = \left(1 - \frac{s_f}{2D}\right)^2. \tag{9}$$

where s_f is the spacing of FRP.

Ultimately, the actual lateral confining stress (f_l) is calculated as shown in Eq. (10).

$$f_l = \frac{2k_\varepsilon k_v E_f \varepsilon_f t_f}{D}. \tag{10}$$

3.1.2 Representative experience model collection

Over the years, various ultimate condition models for FRP-confined concrete have been proposed, divided into design-type and analytical models as classified by Lam and Teng [14]. Design models are based on regression from experimental data, while analytical models use force equilibrium and deformation coordination to estimate FRP–concrete interaction. Ozbakkaloglu et al. [11] found design models generally perform better. Therefore, eight

design models are selected here, detailed in Appendix A in Electronic Supplementary Material [14,25,28–33]. These models feature bilinear stress–strain curves with an initial parabolic rise followed by roughly linear or nonlinear behavior. They apply to circular concrete cylinders fully or partially wrapped with FRP, using common parameters like the axial peak stress of the unconfined cylinder (f_{co}), the axial peak strain of the unconfined cylinder (ε_{co}), f_l, and $\varepsilon_{h,rup}$. The lateral confined stress formula differs by wrapping method: Lam and Teng [14], Jiang and Teng [28], Yan and Pantelides [29], and Binici [30] cover fully wrapped specimens (no invalid confinement area), while Benzaid and Mesbah [31], Pham et al. [32], Guo et al. [25], and Yang et al. [33] apply to partially wrapped specimens considering an invalid area and spacing influence coefficient k_v. Since the database here contains partly wrapped specimens, lateral confined stress f_l is calculated using Eq. (10).

If the FRP confinement exceeds a threshold level, the stress–strain curve shows strain hardening (post-peak rise); if below, it shows strain softening (post-peak drop). Only Jiang and Teng [28], Yan and Pantelides [29], Binici [30], and Yang et al. [33] provide clear predictions for strain softening and thresholds distinguishing hardening from softening. For models predicting only strain-hardening ultimate conditions, $f_{cc} = f_{cu}$. Because strain-softened curves have ultimate strength (f_{cu}) lower than peak strength (f_{cc}), the peak axial strength is used for comparison.

3.2 Database construction

An experimental database of 310 FRP partially confined concrete cylinders is gathered from 15 published publications after a thorough literature review as shown in Appendix B in Electronic Supplementary Material [25,26,32–44]. Some common descriptions of the databases are as follows.

1) This database (in Appendix B in Electronic Supplementary Material [25,26,32–44]) covers the investigations in the recent 16 years, that is from 2008 to 2024.

2) FRP confined concrete cylinders with H/D less than 3 and no reinforcing steel bars, FRP bars, or steel sections within the column.

3) All specimens are wrapped with unidirectional FRP in the hoop direction, and the confinement form is partially wrapped FRP.

4) The core concrete material contains normal strength concrete (NSC, compressive strength less than 55 MPa), high strength concrete (HSC), ultra-high strength concrete (UHSC), ultra-high-performance concrete (UHPC), seawater sea-sand Concrete (SSC) and lightweight aggregate concrete (LWAC), with or without short fiber addition.

5) There is only one loading scenario available: monotonic axial compression. This does not include cyclic axial compression or eccentric compression.

Table 1 shows the statistical features of the maximum and minimum distributions, as well as the mean for each. If not specified by the original publications, the unconfined concrete ultimate strains corresponding to the strengths, are obtained using the following Eq. (11) [45]. Figure 4 shows that the input variable features follow a normal distribution and are suitable for use with a Bayesian optimizer based on a Gaussian distribution.

$$\varepsilon_{co} = 0.0015 + \frac{f_{co}}{70000}. \tag{11}$$

Table 1 Evaluation of database

Variable	Distribution	μ	σ
D (mm)	100–300	149.03	24.12
H (mm)	200–600	300.97	52.59
t_f (mm)	0.05–2.70	0.50	0.38
s_f (mm)	12.5–112.5	52.26	24.78
w (mm)	10–150	36.28	19.50
E_f (GPa)	29.50–249.15	218.73	53.44
$\varepsilon_{h,rup}$ (%)	0.03–2.48	1.14	0.42
f_{co} (MPa)	16.0–122.2	37.18	16.00
ε_{co} (%)	0.139–0.380	0.27	0.07
f_l (MPa)	0.10–55.92	10.22	7.68
f_{cc}/f_{co}	0.91–3.96	1.54	0.48
$\varepsilon_{cc}/\varepsilon_{co}$	0.78–24.14	6.16	4.75

3.3 Identify key physical factors

Variable relationships are visualized using a correlation coefficient matrix and heat map, where color intensity indicates the strength of correlation (range: −1 to 1). Darker shades show strong positive or negative correlations, lighter shades indicate weak or no correlation. As shown in Fig. 5, D and H have a high correlation (0.92), suggesting one could be removed during feature engineering to avoid multicollinearity. Additionally, f_{cc}/f_{co}, $\varepsilon_{cc}/\varepsilon_{co}$ and t_f show relatively strong correlations (0.29), supporting the inclusion of strip spacing in strength prediction. Overall, the selected features are relevant and suitable as model inputs.

4 Results and discussion

4.1 Adaptability bottlenecks of quantitative empirical models in partially constrained data

Figures 6 and 7 show predictions from the empirical

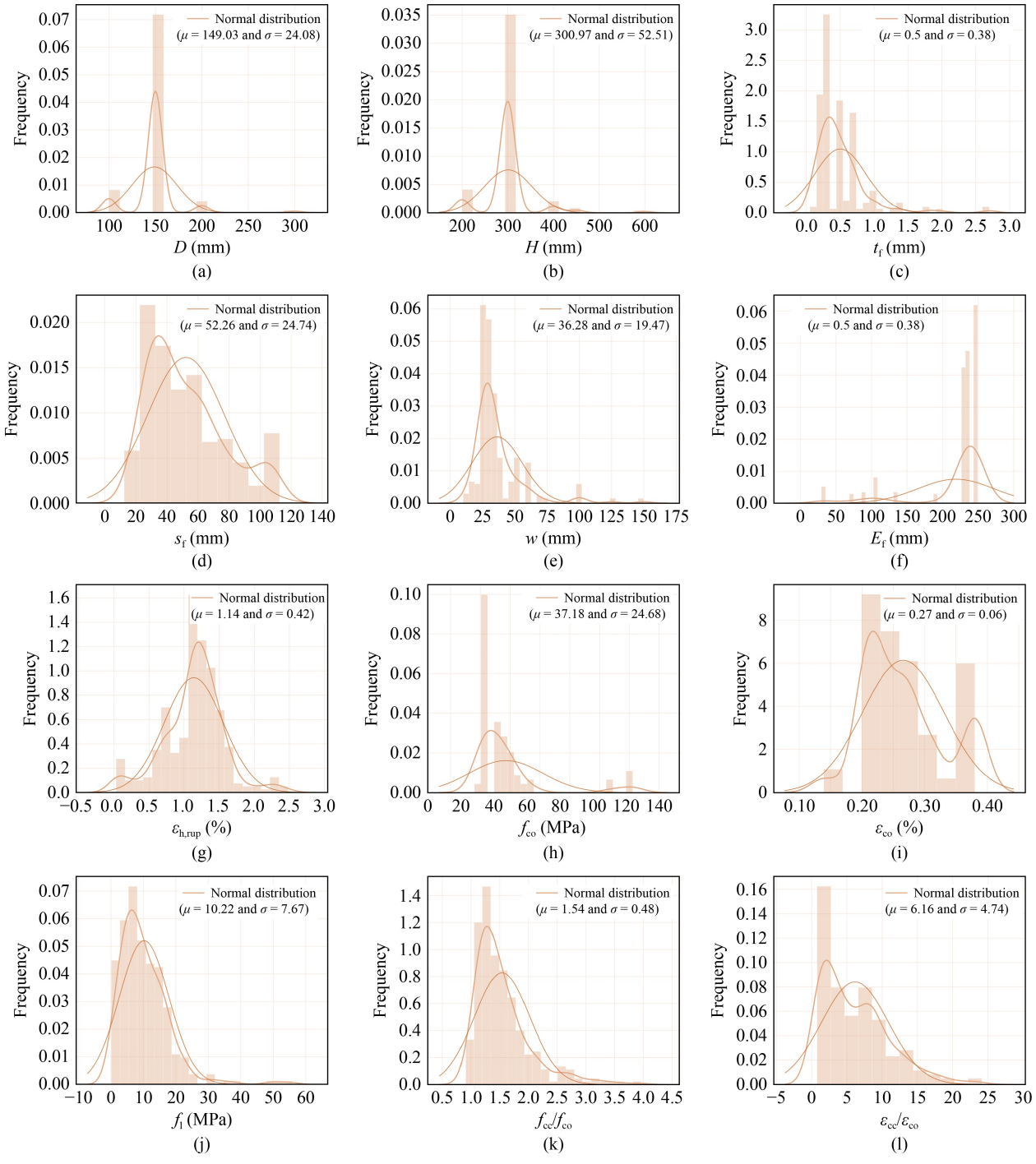

Fig. 4 Normal distribution of GP variables: (a) D (mm) distribution; (b) H (mm) distribution; (c) t_f (mm) distribution; (d) s_f (mm) distribution; (e) w (mm) distribution; (f) E_f (GPa) distribution; (g) $\varepsilon_{h,rup}$ (%) distribution; (h) f_{co} (MPa) distribution; (i) ε_{co} (%) distribution; (j) f_l (MPa) distribution; (k) f_{cc}/f_{co} distribution; (l) $\varepsilon_{cc}/\varepsilon_{co}$ distribution (Note: μ is the mean of value; σ is the sample standard deviation; w is the width of the FRP).

models listed in Appendix A in Electronic Supplementary Material [14,25,28–33], with accuracy assessed by comparing scatter plots and calculated metrics. In the figures, the dashed line shows predicted trends, and the solid line represents perfect predictions; closer alignment indicates higher accuracy. Most models show reasonable performance. For stress predictions, models by Lam and Teng [14], Jiang and Teng [28], Yan and Pantelides [29], Binici [30], Pham et al. [32], and Yang et al. [33] tend to overestimate values, while Benzaid and Mesbah [31] and Guo et al. [25] offer more accurate results. For strain predictions, Lam and Teng [14] and Benzaid and Mesbah [31] are conservative, while Jiang and Teng [28], Yan and Pantelides [29], Binici [30], and Pham et al. [32]

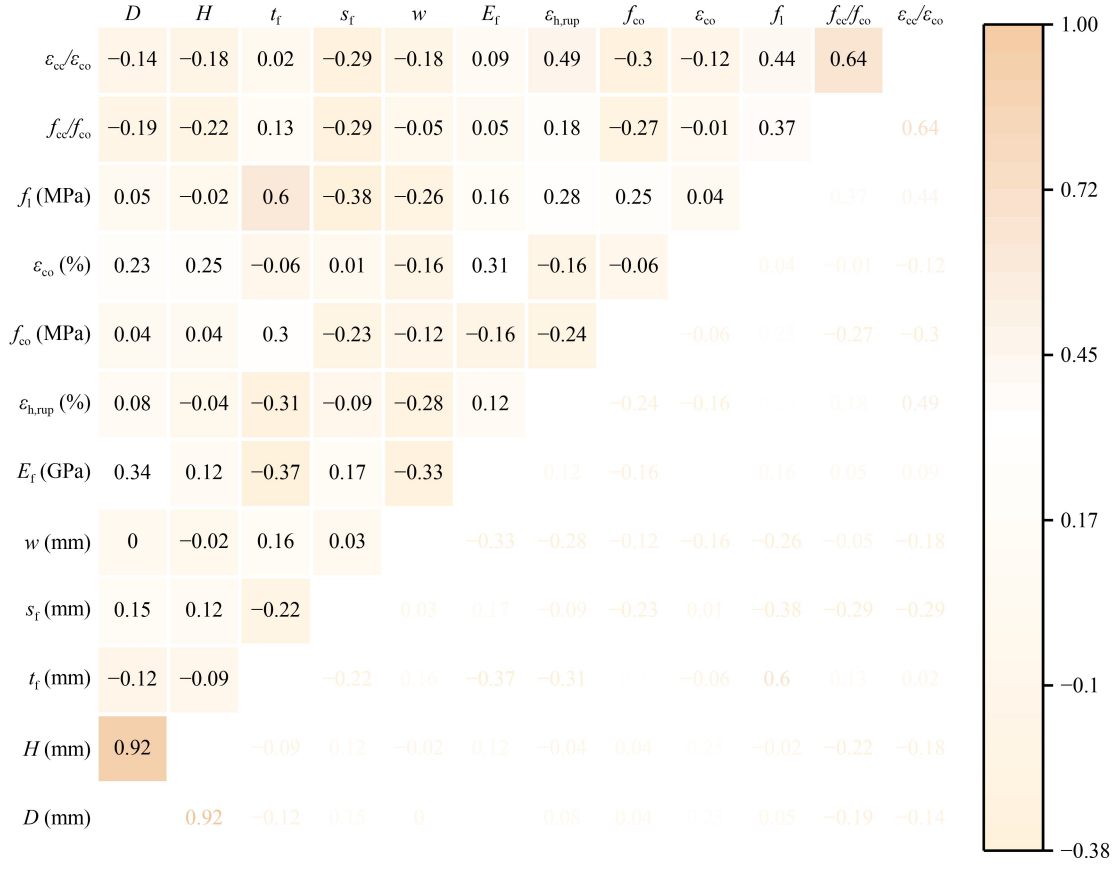

Fig. 5 Key factor correlation heat map.

overpredict; Guo et al. [25] and Yang et al. [33] are more precise.

Metric results in Table 2 support these findings. Guo's model performs best overall in *RMSE*, *CoV*, and *AAE* for both strength and strain, while Benzaid et al.'s [31] model is the only one with *MEAN* < 1, indicating consistently lower predictions. These differences stem from the models' varied formulations and limited data sets,

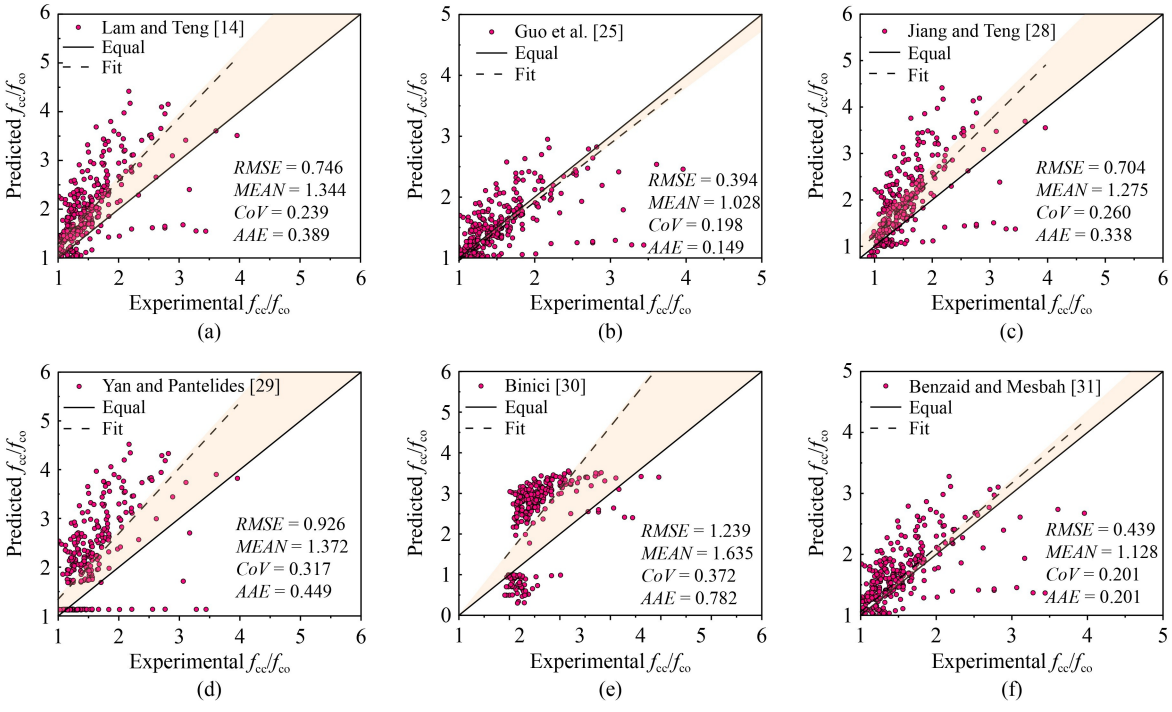

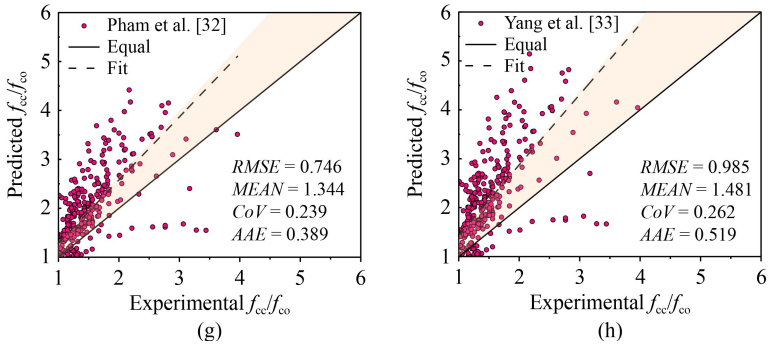

Fig. 6 Experience model f_{cc}/f_{co} prediction verification: (a) Lam and Teng [14]; (b) Guo et al. [25]; (c) Jiang and Teng [28]; (d) Yan and Pantelides [29]; (e) Binici [30]; (f) Benzaid and Mesbah [31]; (g) Pham et al. [32]; (h) Yang et al. [33].

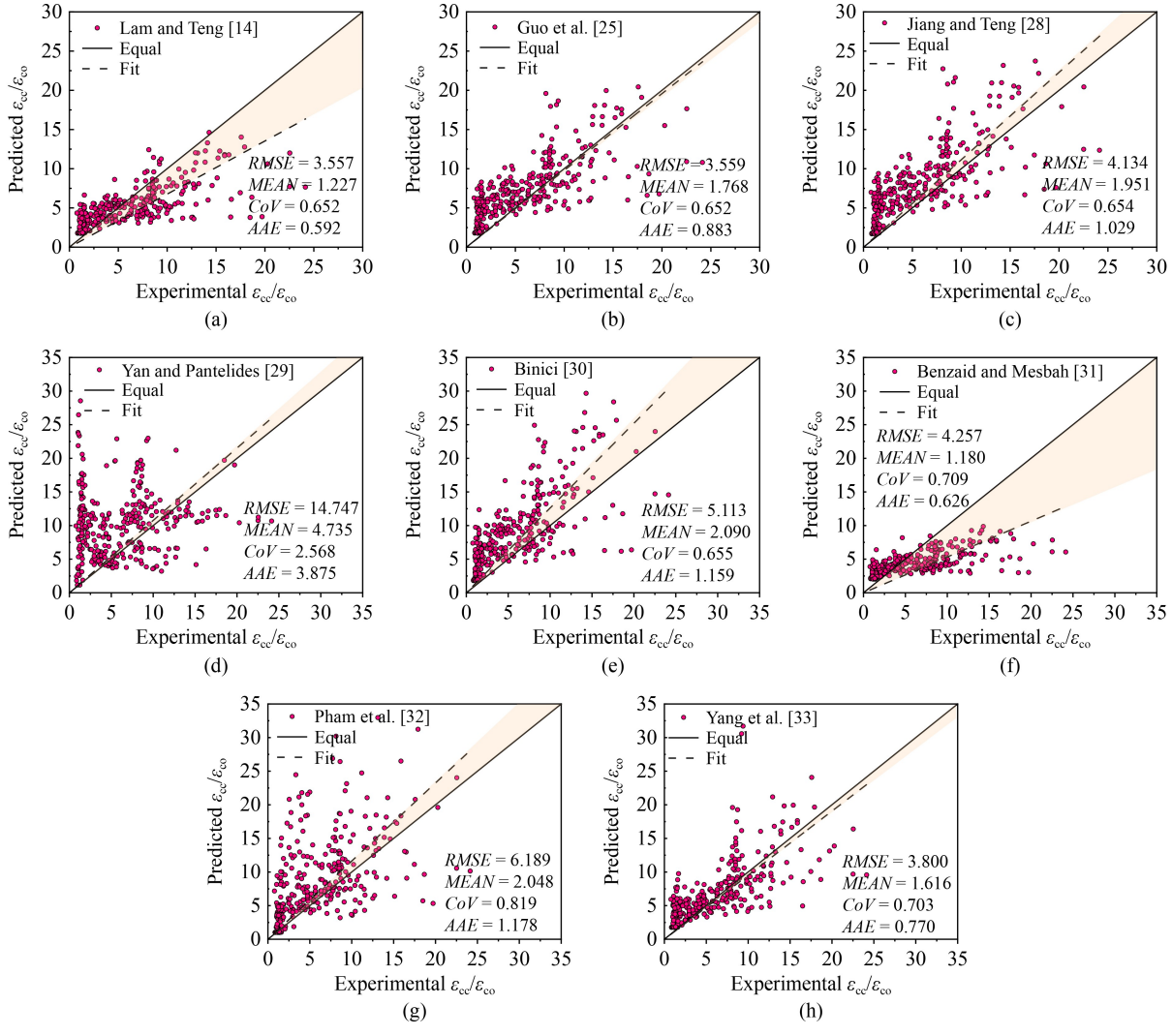

Fig. 7 Experience model $\varepsilon_{cc}/\varepsilon_{co}$ prediction verification: (a) Lam and Teng [14]; (b) Guo et al. [25]; (c) Jiang and Teng [28]; (d) Yan and Pantelides [29]; (e) Binici [30]; (f) Benzaid and Mesbah [31]; (g) Pham et al. [32]; (h) Yang et al. [33].

causing inconsistent performance on broader, more diverse samples. This reveals a key limitation: current empirical models lack generalizability, reducing their practical value in complex or varied engineering scenarios.

4.2 Integrating physical equations and intelligent optimization to solve the problem of robustness in small samples

Based on the proposed methodology, the study first tests XGBoost and RF using default settings. The data set is

Table 2 Error indices for different models

Model	*RMSE*		*MEAN*		*CoV*		*AAE*	
	f_{cc}/f_{co}	$\varepsilon_{cc}/\varepsilon_{co}$	f_{cc}/f_{co}	$\varepsilon_{cc}/\varepsilon_{co}$	f_{cc}/f_{co}	$\varepsilon_{cc}/\varepsilon_{co}$	f_{cc}/f_{co}	$\varepsilon_{cc}/\varepsilon_{co}$
Lam and Teng [14]	0.75	3.56	1.34	1.23	0.24	0.65	0.39	0.59
Guo et al. [25]	0.40	3.56	1.03	1.77	0.20	0.65	0.15	0.88
Jiang and Teng [28]	0.70	4.13	1.28	1.95	0.26	0.65	0.34	1.03
Yan and Pantelides [29]	0.93	14.75	1.37	4.74	0.32	2.57	0.45	3.88
Binici [30]	1.24	5.11	1.64	2.09	0.37	0.66	0.78	1.16
Benzaid and Mesbah [31]	1.13	4.26	0.20	0.78	0.20	0.71	12.48	0.63
Pham et al. [32]	0.75	6.19	1.34	2.05	0.24	0.82	0.39	1.18
Yang et al. [33]	0.99	3.80	1.48	1.62	0.26	0.70	0.52	0.77
XGBoost	0.16	2.79	1.02	1.40	0.06	0.38	0.08	0.52
RF	0.17	2.60	1.03	1.47	0.05	0.38	0.08	0.56
XGBoost−BO	0.11	2.26	1.02	1.35	0.04	0.36	0.06	0.50
RF−BO	0.20	1.9	1.04	1.23	0.06	0.34	0.10	0.31

split into training and test sets, with model accuracy evaluated using four standard metrics. BO is then used to tune hyperparameters within set ranges, combined with internal *K*-fold cross-validation to ensure reliable model selection. In *K*-fold CV, the data are divided into *K* parts; each subset is used once for validation and $K-1$ times for training, with average error as the final performance. This approach improves data efficiency and stability. Here, 5-fold CV is used, and all workflows are conducted in Python (Jupyter Notebook). The optimized parameters are listed in Table 3.

To improve robustness and generalization on small, noisy data sets, this study combines PIML with Bayesian hyperparameter optimization. Figures 8 and 9 show prediction results before and after optimization; Table 2 presents *RMSE, MEAN*, *CoV*, and *AAE* metrics. All models perform close to the 1:1 ideal line, indicating no major bias and confirming strong baseline accuracy. Notably, performance improves further with BO tuning, which effectively searches the hyperparameter space. The Bayesian-optimized XGBoost (XGBoost–BO) achieved the best prediction for the strength ratio f_{cc}/f_{co}, with *RMSE* = 0.112, *MEAN* = 1.017, *CoV* = 0.687, and *AAE* = 0.059, indicating high accuracy and low error dispersion. The default XGBoost had similar *MEAN* but higher *RMSE* and *CoV*, showing optimization further improves stability. In contrast, RF–BO performed worst for f_{cc}/f_{co}, likely due to insufficient hyperparameter tuning. However, for the strain ratio $\varepsilon_{cc}/\varepsilon_{co}$, RF–BO outperformed all models (*RMSE* = 1.922, *AAE* = 0.312), suggesting simple models can still excel with proper tuning. These results confirm that combining physics-informed loss functions with BO enhances accuracy and generalization, offering a practical solution for reliable predictions in small or noisy structural data sets.

Table 3 The optimal hyperparametric combination

Type	Hyperparameter	Result
XGBoost	n_estimators	190
	max_depth	8
	learn_rate	0.13
	gamma	0.05
	reg_alpha	0.03
	reg_lambda	0.76
	min_child_weight	4
	subsample	0.57
	colsample_bytree	0.8
RF	n_estimators	136
	max_depth	6
	max_feature	18

4.3 Verifying the effectiveness of physical embedding in noise suppression

To evaluate the effect of physical embedding on reducing noise and improving robustness, a Taylor diagram (Fig. 10) was used to compare empirical models and ML approaches, with and without optimization. In this diagram, each point represents a model; the distance, angle, and arcs denote standard deviation, correlation coefficient, and *RMSE*, respectively. Models closer to the reference point show better accuracy and lower variance. For the strength ratio f_{cc}/f_{co}, all ML models clustered near the 0.2 *RMSE* arc, indicating low error. The best performance came from the physics-informed XGBoost with Bayesian optimization, showing minimal deviation. In contrast, empirical models spread between the 0.4 and 0.8 arcs, reflecting higher and inconsistent errors. A similar pattern was observed for $\varepsilon_{cc}/\varepsilon_{co}$, where the

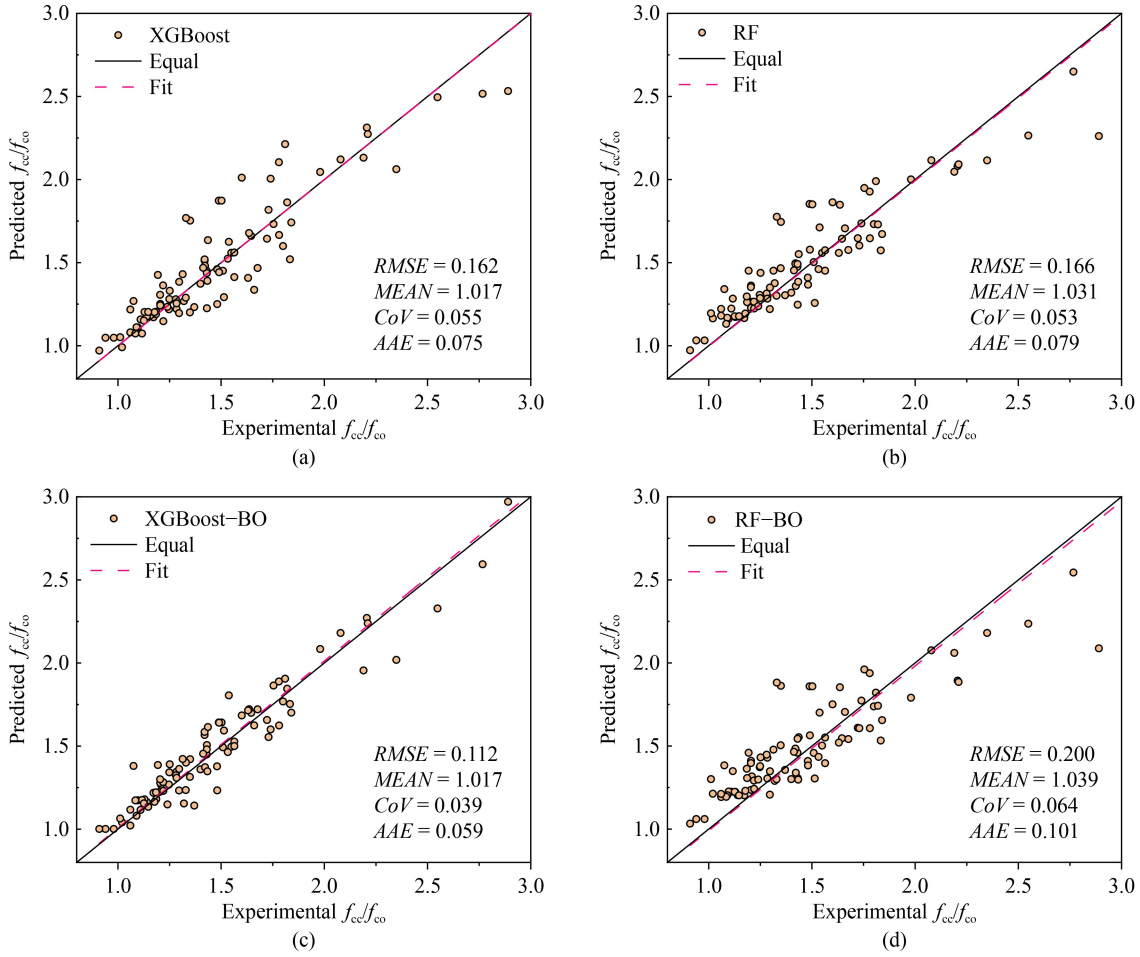

Fig. 8 PIML model f_{cc}/f_{co} prediction verification: (a) XGBoost; (b) RF; (c) XGBoost–BO; (d) RF–BO.

RF–BO model stood out among ML methods. Overall, ML models, especially those with physical constraints, aligned well with experimental data, showing high correlation and improved generalization. This confirms that embedding physical knowledge reduces overfitting and enhances stability. The analysis supports the development of hybrid predictive equations that blend ML precision with physical interpretability for FRP-confined concrete design.

4.4 Revealing the physically dominant features on which physics-informed machine learning models depend

To identify key physical drivers behind PIML predictions, a feature importance analysis was conducted using XGBoost. Feature contributions were quantified via the feature_importances_ attribute from Scikit-learn, based on how often each variable was used in tree splits. As shown in Fig. 11, nine input features were evaluated for

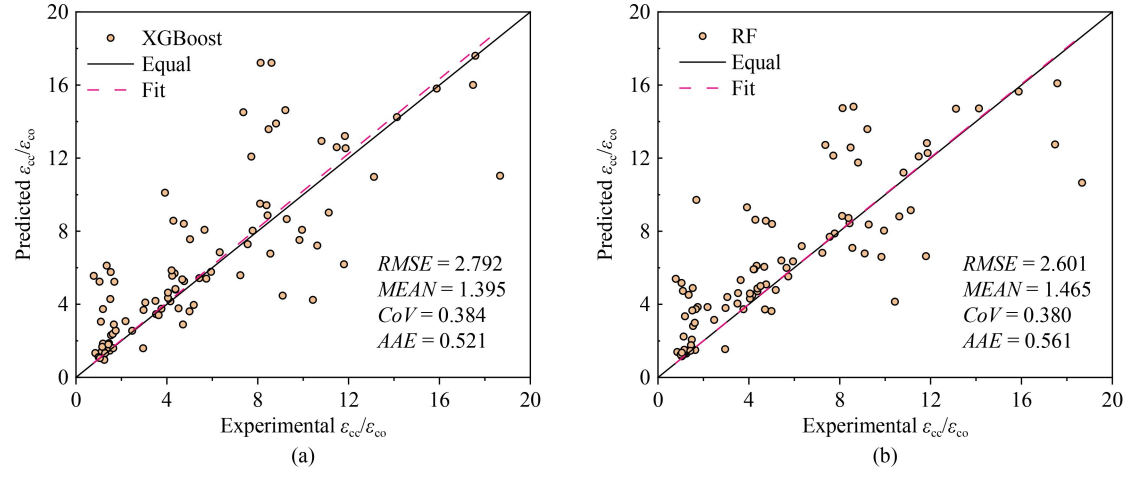

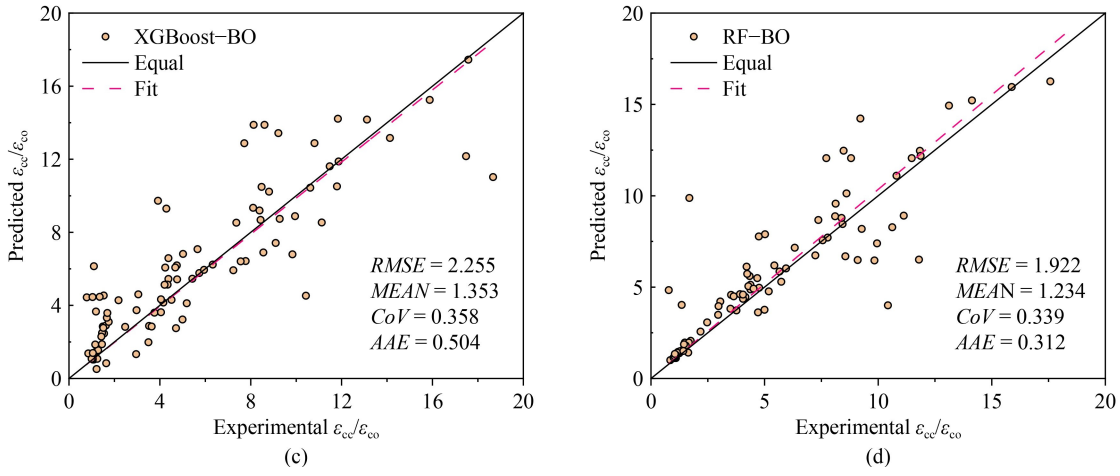

Fig. 9 PIML model $\varepsilon_{cc}/\varepsilon_{co}$ prediction verification: (a) XGBoost; (b) RF; (c) XGBoost–BO; (d) RF–BO.

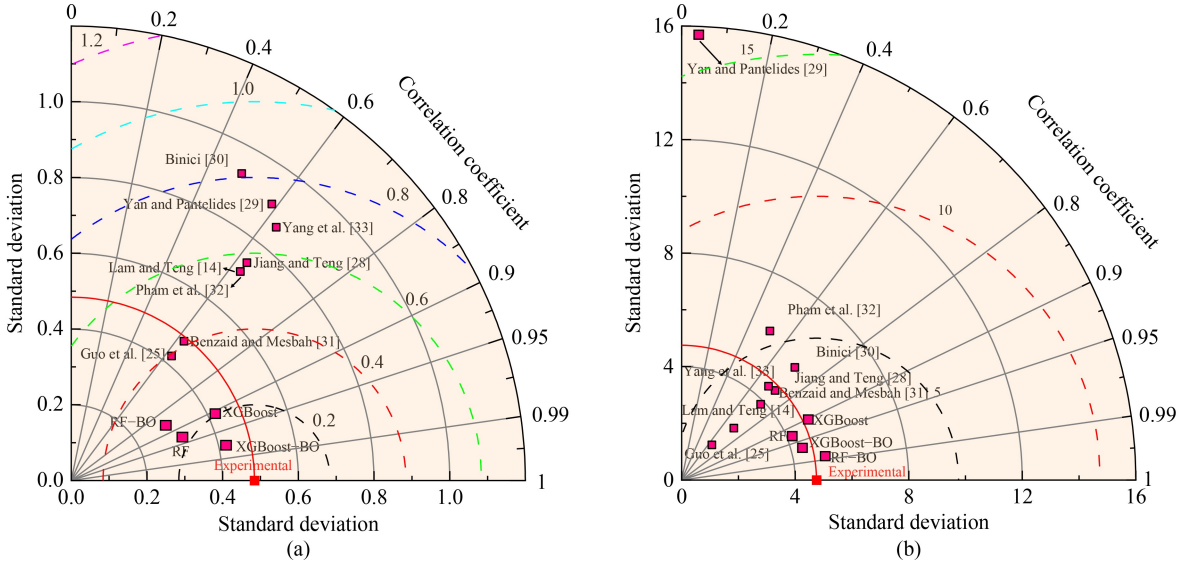

Fig. 10 Taylor diagram for error analysis: (a) f_{cc}/f_{co}; (b) $\varepsilon_{cc}/\varepsilon_{co}$.

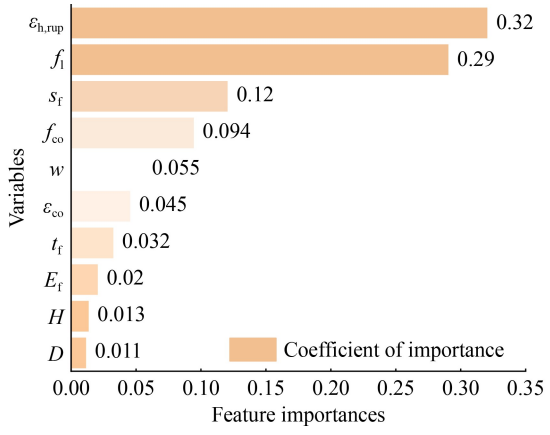

Fig. 11 Features importance analysis.

their influence on predicted strength and strain ratios (f_{cc}/f_{co}, $\varepsilon_{cc}/\varepsilon_{co}$). The hoop rupture strain $\varepsilon_{cc}/\varepsilon_{co}$ had the highest importance (0.32), followed by lateral stress f_l and strip spacing s_f, reflecting their strong link to FRP confinement efficiency. Geometric parameters D and H showed the least influence, likely due to limited variation in cross-sectional size and omission of the H/D ratio. Overall, the PIML model emphasizes physically relevant features, confirming that embedding domain knowledge enhances both accuracy and interpretability.

4.5 Engineering the expression of artificial intelligence (AI) driven knowledge

The above study demonstrates that the ML model can better predict the design of FRP partially confined concrete cylinders ultimate conditions. ML training models are black-box functions with great accuracy. However, the underlying workings of these models are difficult to understand, and it is impossible to see the form of the displayed equations. To assist the design of the ultimate conditions of FRP partially confined concrete

cylinders, we develop an explicit equation based on the ML model's accurate prediction findings. We use the first six parameters from the parameter importance analysis in Subsection 4.4, and the new explicit equation is Eqs. (12) and (13), which is based on the prior ultimate conditional equations in Appendix A in Electronic Supplementary Material [14,25,28–33].

$$\frac{f_{cc}}{f_{co}} = F_1\left(\frac{\varepsilon_{h,rup}}{\varepsilon_{co}}\right)F_2\left(\frac{f_l}{f_{co}}\right)F_3\left(\frac{s_f}{w}\right), \tag{12}$$

$$\frac{\varepsilon_{cc}}{\varepsilon_{co}} = Z_1\left(\frac{\varepsilon_{h,rup}}{\varepsilon_{co}}\right)Z_2\left(\frac{f_l}{f_{co}}\right)Z_3\left(\frac{s_f}{w}\right), \tag{13}$$

where $F_1\left(\frac{\varepsilon_{h,rup}}{\varepsilon_{co}}\right) = \alpha_1\left(\frac{\varepsilon_{h,rup}}{\varepsilon_{co}}\right)^{\beta_1^a}$, $F_2(\frac{f_l}{f_{co}}) = \alpha_2\left(\frac{f_l}{f_{co}} - \alpha_3\right)^{\beta_2}$ and $F_3(\frac{s_f}{w}) = \alpha_4\left(\frac{s_f}{w}\right)^{\beta_3}$, and $Z_1\left(\frac{\varepsilon_{h,rup}}{\varepsilon_{co}}\right) = \alpha_5\left(\frac{\varepsilon_{h,rup}}{\varepsilon_{co}}\right)^{\beta_4}$, $Z_2(\frac{f_l}{f_{co}}) = \alpha_6\left(\frac{f_l}{f_{co}} - \alpha_7\right)^{\beta_5}$ and $Z_3\left(\frac{s_f}{w}\right) = \alpha_8\left(\frac{s_f}{w}\right)^{\beta_6}$, and α_1, α_2, α_3, α_4, α_5, α_6, α_7, α_8, β_1^a, β_2, β_3, β_4, β_5, β_6 are parameters to be determined based on the prediction data of the trained ML models.

It is possible to estimate FRP partially confined concrete cylinders ultimate conditions for various combinations of input parameters using the trained ML model, given the standard values. Based primarily on the median number of each parameter in the database, as indicated by Table 4, the reduced database determined the standard value for each of the input parameters of Eqs. (12) and (13). The comparison results in Subsection 4.3 reveal that the Bayesian-optimized XGBoost model is more accurate, so we employed the XGBoost training model for curve equation fitting with the following steps.

First, the standard parameters of $\frac{f_l}{f_{co}} = 0.292$, and $\frac{s_f}{w} = 1.458$ were introduced into the trained XGBoost model, and $\varepsilon_{h,rup}$ and ε_{co} were changed equally across the database. Figures 12(a) and 12(d) show a comparison of $\frac{f_{cc}}{f_{co}}$, $\frac{\varepsilon_{cc}}{\varepsilon_{co}}$ and $\frac{\varepsilon_{h,rup}}{\varepsilon_{co}}$. The curve fitting of the predicted results of the $\frac{f_{cc}}{f_{co}}$, $\frac{\varepsilon_{cc}}{\varepsilon_{co}}$ and $\frac{\varepsilon_{h,rup}}{\varepsilon_{co}}$ relationship yields to:

$$X_1\left(\frac{\varepsilon_{h,rup}}{\varepsilon_{co}}\right) = \frac{f_{cc}}{f_{co}} = F_2(0.292)\,F_3(1.458) = 1.268\left(\frac{\varepsilon_{h,rup}}{\varepsilon_{co}}\right)^{0.125}, \tag{14}$$

$$Y_1\left(\frac{\varepsilon_{h,rup}}{\varepsilon_{co}}\right) = \frac{\varepsilon_{cc}}{\varepsilon_{co}} = Z_2(0.292)\,Z_3(1.458) = 0.046\left(\frac{\varepsilon_{h,rup}}{\varepsilon_{co}}\right)^{3.101}. \tag{15}$$

The fitting has a R^2 of 0.965 and 0.877. The functional equations F_1 and Z_1 with regard to $\frac{\varepsilon_{h,rup}}{\varepsilon_{co}}$ are shown in

Table 4 Limit values and standard values for the input parameters

Variable	Min	Max	Standard value
$\varepsilon_{h,rup}$ (%)	0.04	2.17	1.16
f_l (MPa)	0.11	51.90	9.43
s_f (mm)	12.50	112.50	43.75
f_{co} (MPa)	23.00	122.20	32.30
w (mm)	15.00	150.00	30.00
ε_{co} (%)	0.14	0.38	0.26

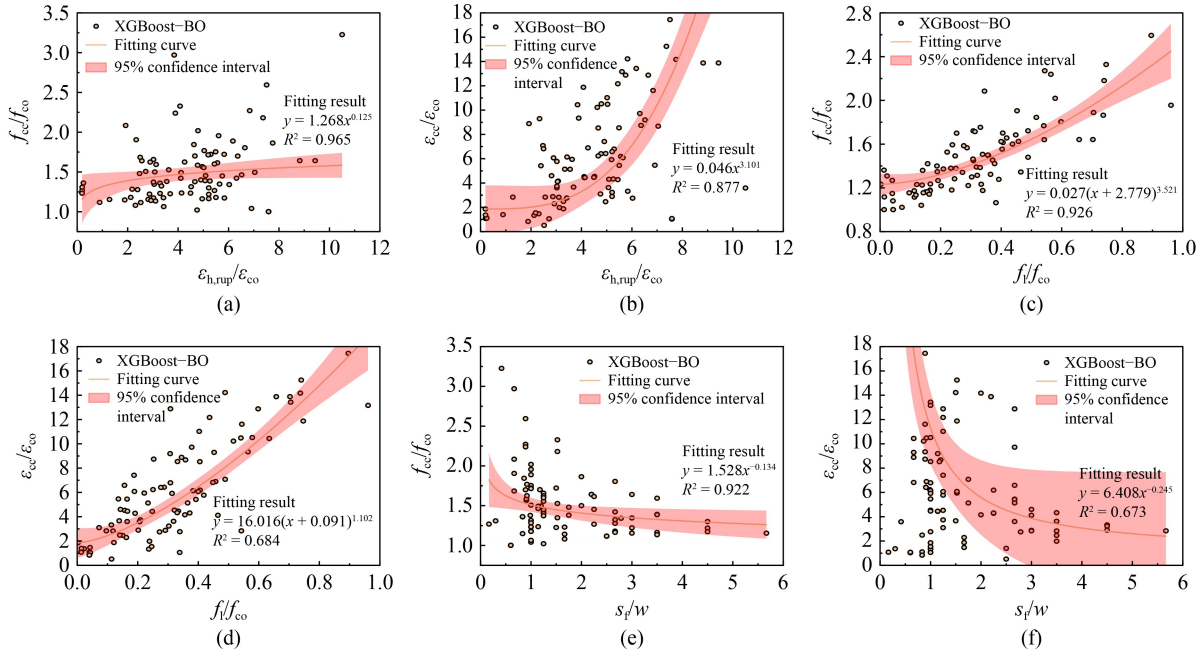

Fig. 12 Fitting curve of explicit formula: (a) $\frac{f_{cc}}{f_{co}} - \frac{\varepsilon_{h,rup}}{\varepsilon_{co}}$; (b) $\frac{\varepsilon_{cc}}{\varepsilon_{co}} - \frac{\varepsilon_{h,rup}}{\varepsilon_{co}}$; (c) $\frac{f_{cc}}{f_{co}} - \frac{f_l}{f_{co}}$; (d) $\frac{\varepsilon_{cc}}{\varepsilon_{co}} - \frac{f_l}{f_{co}}$; (e) $\frac{f_{cc}}{f_{co}} - \frac{s_f}{w}$; (f) $\frac{\varepsilon_{cc}}{\varepsilon_{co}} - \frac{s_f}{w}$.

Eqs. (16) and (17).

$$F_1\left(\frac{\varepsilon_{\mathrm{h,rup}}}{\varepsilon_{\mathrm{co}}}\right)=\frac{X_1\left(\dfrac{\varepsilon_{\mathrm{h,rup}}}{\varepsilon_{\mathrm{co}}}\right)}{F_2(0.292)\,F_3(1.458)}, \tag{16}$$

$$Z_1\left(\frac{\varepsilon_{\mathrm{h,rup}}}{\varepsilon_{\mathrm{co}}}\right)=\frac{Y_1\left(\dfrac{\varepsilon_{\mathrm{h,rup}}}{\varepsilon_{\mathrm{co}}}\right)}{Z_2(0.292)\,Z_3(1.458)}. \tag{17}$$

Using the same procedure above, the relationship between $\frac{f_{\mathrm{cc}}}{f_{\mathrm{co}}}$, $\frac{\varepsilon_{\mathrm{cc}}}{\varepsilon_{\mathrm{co}}}$ and $\frac{f_{\mathrm{l}}}{f_{\mathrm{co}}}$ were fitted as:

$$X_2\left(\frac{f_{\mathrm{l}}}{f_{\mathrm{co}}}\right)=\frac{f_{\mathrm{cc}}}{f_{\mathrm{co}}}=F_1(4.46)\,F_3(1.458)=0.027\left(\frac{f_{\mathrm{l}}}{f_{\mathrm{co}}}+2.079\right)^{4.521}, \tag{18}$$

$$Y_2\left(\frac{f_{\mathrm{l}}}{f_{\mathrm{co}}}\right)=\frac{\varepsilon_{\mathrm{cc}}}{\varepsilon_{\mathrm{co}}}=Z_1(4.46)\,Z_3(1.458)=16.016\left(\frac{f_{\mathrm{l}}}{f_{\mathrm{co}}}+0.091\right)^{1.102}. \tag{19}$$

The comparison between Eqs. (18) and (19) the prediction data are shown in Figs. 12(b) and 12(e). The fitting has a R^2 of 0.926 and 0.684. Equations (18) and (19) give:

$$F_2\left(\frac{f_{\mathrm{l}}}{f_{\mathrm{co}}}\right)=\frac{X_2\left(\dfrac{f_{\mathrm{l}}}{f_{\mathrm{co}}}\right)}{F_1(4.46)\,F_3(1.458)}, \tag{20}$$

$$Z_2\left(\frac{f_{\mathrm{l}}}{f_{\mathrm{co}}}\right)=\frac{Y_2\left(\dfrac{f_{\mathrm{l}}}{f_{\mathrm{co}}}\right)}{Z_1(4.46)\,Z_3(1.458)}. \tag{21}$$

Using the same procedure, the relationship between $\frac{f_{\mathrm{cc}}}{f_{\mathrm{co}}}$, $\frac{\varepsilon_{\mathrm{cc}}}{\varepsilon_{\mathrm{co}}}$ and $\frac{s_{\mathrm{f}}}{w}$ were fitted as:

$$X_3\left(\frac{s_{\mathrm{f}}}{w}\right)=\frac{f_{\mathrm{cc}}}{f_{\mathrm{co}}}=F_1(4.46)\,F_2(0.292)=1.528\left(\frac{s_{\mathrm{f}}}{w}\right)^{-0.134}, \tag{22}$$

$$Y_3\left(\frac{s_{\mathrm{f}}}{w}\right)=\frac{\varepsilon_{\mathrm{cc}}}{\varepsilon_{\mathrm{co}}}=Z_1(4.46)\,Z_2(0.292)=6.408\left(\frac{s_{\mathrm{f}}}{w}\right)^{-0.245}. \tag{23}$$

The comparison between Eqs. (22) and (23) the prediction data are shown in Figs. 12(c) and 12(f). The fitting has a R^2 of 0.922 and 0.673. Equations (22) and (23) give:

$$F_3\left(\frac{s_{\mathrm{f}}}{w}\right)=\frac{X_2\left(\dfrac{s_{\mathrm{f}}}{w}\right)}{F_1(4.46)\,F_2(0.292)}, \tag{24}$$

$$Z_3\left(\frac{s_{\mathrm{f}}}{w}\right)=\frac{Y_2\left(\dfrac{s_{\mathrm{f}}}{w}\right)}{Z_1(4.46)\,Z_2(0.292)}. \tag{25}$$

Considering the standard value of the parameters (Table 4), $\varepsilon_{\mathrm{h,rup}}=1.16\%$, $f_{\mathrm{l}}=9.43$ MPa, $s_{\mathrm{f}}=43.75$ mm, $f_{\mathrm{co}}=32.3$ MPa, $\varepsilon_{\mathrm{co}}=0.26\%$, and $w=30$ mm, the results are $\frac{1}{F_1(4.46)^2F_2(0.292)^2F_3(1.428)^2}=0.510$, and $\frac{1}{Z_1(4.46)^2Z_2(0.292)^2Z_3(1.428)^2}=0.038$. Finally, Eqs. (26) and (27) were obtained:

$$\frac{f_{\mathrm{cc}}}{f_{\mathrm{co}}}=0.510X_1\left(\frac{\varepsilon_{\mathrm{h,rup}}}{\varepsilon_{\mathrm{co}}}\right)X_2\left(\frac{f_{\mathrm{l}}}{f_{\mathrm{co}}}\right)X_3\left(\frac{s_{\mathrm{f}}}{w}\right), \tag{26}$$

$$\frac{\varepsilon_{\mathrm{cc}}}{\varepsilon_{\mathrm{co}}}=0.038Y_1\left(\frac{\varepsilon_{\mathrm{h,rup}}}{\varepsilon_{\mathrm{co}}}\right)Y_2\left(\frac{f_{\mathrm{l}}}{f_{\mathrm{co}}}\right)Y_3\left(\frac{s_{\mathrm{f}}}{w}\right). \tag{27}$$

To make ML predictions more interpretable for engineering use, this study derives empirical equations (Eqs. (26) and (27)) based on key features identified by the AI model. Figure 13 shows their performance in predicting normalized axial stress $f_{\mathrm{cc}}/f_{\mathrm{co}}$ and strain $\varepsilon_{\mathrm{cc}}/\varepsilon_{\mathrm{co}}$ on the test set. The y-axis shows the Experimental-to-New equation (E/N) ratio, and the x-axis shows sample indices. The black dotted line at $y=1.0$ indicates perfect prediction. Data points are evenly distributed around this line, especially for strain, showing that the equations capture the main trends well. Four metrics from Subsection 2.5, *RMSE*, *MEAN*, *CoV*, and *AAE*, quantify performance. For stress, the results are (0.648, 1.133, 0.306, 0.263), and for strain (21.652, 2.622, 2.161, 2.140). Although accuracy is slightly lower than the original ML models, the new equations still outperform many existing empirical models. More importantly, they offer a clear balance between accuracy and interpretability. By converting complex AI-learned patterns into explicit formulas, these equations help bridge the gap between data-driven insights and practical engineering use, supporting design and code development.

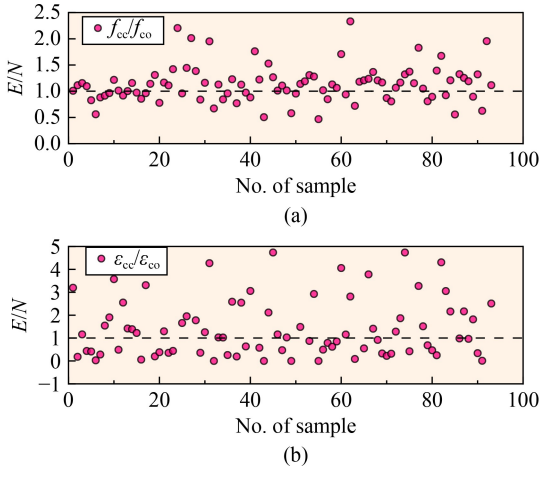

Fig. 13 Verification of explicit equation accuracy: (a) $f_{\mathrm{cc}}/f_{\mathrm{co}}$; (b) $\varepsilon_{\mathrm{cc}}/\varepsilon_{\mathrm{co}}$.

5 Conclusions

This study is based on experimental data from 310 groups of FRP-constrained cylindrical columns. By employing a loss function embedded with physical information, Bayesian hyperparameter optimization, and *K*-fold cross-validation of the XGBoost/RF algorithm, a PIML framework was ultimately constructed, which may enable a transition from empirical estimation to physical intelligent robot design layout in the design of FRP-constrained columns in civil/industrial buildings. The specific conclusions are as follows.

1) The PIML model developed in this study significantly improves prediction accuracy. The optimized XGBoost and RF models reduce the prediction error (*RMSE*) to 0.112–2.255, a 47.70% reduction compared to empirical models, while explicit equations reduce the *RMSE* by 7.95%.

2) The PIML model significantly improves generalization ability on small sample data. Optimization significantly reduces the *RMSE* of XGBoost/RF to (0.112, 0.200) and (2.255, 1.922), with a 32% improvement in generalization ability. The parameter importance analysis reveals that the dominant laws of physics: $\varepsilon_{h,rup}$ (0.32), s_f (0.29) and f_l (0.12) constitute the core decision-making factors.

3) The PIML model significantly improves the interpretability of black-box functions. The axial stress–strain equation is innovatively embedded in the loss function, and the physical constraints improve the consistency of model predictions with mechanical principles by 41%.

The PIML framework greatly improves accuracy but faces three limitations: 1) data mainly involve carbon fiber reinforced polymer (CFRP), lacking validation for other FRPs and ultra-high-strength concrete; 2) physical constraints only use axial models, ignoring interface damage; 3) explicit equations show 12.5% error when $(s_f/w) > 3$. Future work will integrate digital image correlation (DIC) and acoustic data into models and develop adaptive winding robots for real-time prediction and control.

Electronic Supplementary Material Supplementary material is available in the online version of this article at https://doi.org/10.1007/s11709-026-1295-7 and is accessible for authorized users.

Acknowledgements This work was financially supported by Fundamental Research Fund of Natural Science Foundation of China (52208434), Key R&D projects in Henan Province (251111322400), Henan Provincial Higher Education Young Key Teacher Talent Program (2025-56), Talent Development Program for Innovation at Henan University of Technology (21421347), National Key Laboratory for Safety and Resilience in Civil Engineering in Mountainous Areas (SQQZ2025112), Science and Technology Project of Henan Communications Investment Group Co., Ltd. (HNJT2024-37), Science Foundation Projects of Fujian Province (2023J01282).

Competing interests The authors declare that they have no competing interests.

References

1. Yuan W, Jia Z, Hu M, Han Q, Liao W, Bai Y. Seismic behavior of bridge columns with FRP-reinforced ECC at plastic hinge zones. Engineering Structures, 2025, 338: 120573
2. Chen C, Liang T, Zhou Y, Cheng L, Zhang L. Shear resisting mechanisms of ECC FRP strengthened RC beams. Journal of Composites for Construction, 2024, 28(5): 04024038
3. Khodadadi N, Roghani H, Harati E, Mirdarsoltany M, de Caso F, Nanni A. Fiber-reinforced polymer (FRP) in concrete: A comprehensive survey. Construction and Building Materials, 2024, 432: 136634
4. Hammad M, Bahrami A, Khokhar S A, Khushnood R A. A state-of-the-art review on structural strengthening techniques with FRPs: Effectiveness, shortcomings, and future research directions. Materials, 2024, 17(6): 1408
5. Chu C, Liu B, Xu W, Liu H. Axial compressive behavior of short columns of BFRP strip-PVC tube composite reinforced fiber recycled concrete. Structures, 2024, 67: 106983
6. Ghasri M, Ghasemi M, Salarnia A. Leveraging the power of hybrid and standalone machine learning for enhanced FRP-confined concrete columns strength prediction. Journal of Soft Computing in Civil Engineering, 2025, 9(3): 60–96
7. Zeng J J, Xiang H Y, Cai W J, Zhou J K, Zhuge Y, Zhu J Y. Behavior of large-scale FRP-confined square RC columns with UHP-ECC section curvilinearization under eccentric compression. Engineering Structures, 2024, 301: 117288
8. Wang J, Xiao H, Lu L, Yang J, Lu S, Shayanfar J. Axial stress–strain model for concrete in partially FRP wrapped reinforced concrete columns. Construction and Building Materials, 2024, 416: 135028
9. Shayanfar J, Barros J A, Rezazadeh M. Stress–strain model for FRP-confined circular concrete columns developing structural softening behavior. Journal of Composites for Construction, 2024, 28(1): 04023065
10. Li P D, Gao S J, Wu Y F. Stress distribution in concrete with nonuniform passive FRP confinement. Journal of Composites for Construction, 2024, 28(6): 04024052
11. Ozbakkaloglu T, Lim J C, Vincent T. FRP-confined concrete in circular sections: Review and assessment of stress–strain models. Engineering Structures, 2013, 49: 1068–1088
12. Zhang Y, Ren C, Qian L, Wei Y, Liu J, Li G. Machine learning-based capacity model for CFST columns with damaged BFRP jackets. Composite Structures, 2025, 362: 119120
13. Liu X, Sun G, Ju R, Li J, Li Z, Jiang Y, Zhao K, Zhang Y, Jing Y, Yang G. Prediction of load-bearing capacity of FRP-steel composite tubed concrete columns: Using explainable machine learning model with limited data. Structures, 2025, 71: 107890
14. Lam L, Teng J G. Design-oriented stress–strain model for FRP-confined concrete. Construction and Building Materials, 2003, 17(6–7): 471–489
15. Bian K, Priyadarshi R. Machine learning optimization techniques: A survey, classification, challenges, and future research issues.

Archives of Computational Methods in Engineering, 2024, 31(7): 4209–4233
16. Hu T, Zhang H, Cheng C, Li H, Zhou J. Explainable machine learning: Compressive strength prediction of FRP-confined concrete column. Materials Today: Communications, 2024, 39: 108883
17. Ghani M U, Ahmad N, Abraha K G, Manj R Z A, Sharif M H, Wei L. Review and assessment of material, method, and predictive modeling for fiber-reinforced polymer (FRP) partially confined concrete columns. Polymers, 2024, 16(10): 1367
18. Koodiani H K, Erfanian N, Majlesi A, Hosseinzadeh A, Jafari E, Shahin M, Matamoros A. Calibrating equations to predict the compressive strength of FRP-Confined columns using optimized neural network model. Structures, 2023, 56: 105060
19. Zhang F, Wang C, Liu J, Zou X, Sneed L H, Bao Y, Wang L. Prediction of FRP-concrete interfacial bond strength based on machine learning. Engineering Structures, 2023, 274: 115156
20. Yue C, Isleem H F, Qader D N, Mahmoudian A, Weiming T, Jangir P, Arpita, Hamed A Y. Utilization finite element and machine learning methods to investigation the axial compressive behavior of elliptical FRP-confined concrete columns. Structures, 2024, 70: 107681
21. Chen W, Xu J, Yu K, Yu J, Ma M, Ma Z. Performance-based design of FRP-confined recycled aggregate concrete powered by machine learning techniques. Engineering Structures, 2025, 336: 120478
22. Yang D, Lin S, Zhao Y G. Components interaction mechanism and strength of axially loaded FRP-confined concrete stub columns from energy path perspective. Structures, 2025, 71: 107981
23. Zhong S, Zhang L, Zhu J. A path-dependent stress–strain model of FRP-confined circular concrete columns derived from an energy balance approach. Engineering Structures, 2024, 321: 118919
24. Pessiki S, Harries K A, Kestner J T, Sause R, Ricles J M. Axial behavior of reinforced concrete columns confined with FRP jackets. Journal of Composites for Construction, 2001, 5(4): 237–245
25. Guo Y C, Gao W Y, Zeng J J, Duan Z J, Ni X Y, Peng K D. Compressive behavior of FRP ring-confined concrete in circular columns: Effects of specimen size and a new design-oriented stress–strain model. Construction and Building Materials, 2019, 201: 350–368
26. Zeng J J, Guo Y C, Gao W Y, Chen W P, Li L J. Stress–strain behavior of concrete in circular concrete columns partially wrapped with FRP strips. Composite Structures, 2018, 200: 810–828
27. Zeng J J, Duan Z J, Guo Y C, Xie Z H, Li L J. Novel fiber-reinforced polymer cross wrapping strengthening technique: A comparative study. Advances in Structural Engineering, 2020, 23(5): 979–996
28. Jiang T, Teng J. Strengthening of short circular RC columns with FRP jackets: A design proposal. In: Proceedings of the third International Conference on FRP Composites in Civil Engineering (CICE 2006). Miami, FL: International Institute for FRP in Construction, 2006
29. Yan Z, Pantelides C P. Design-oriented model for concrete columns confined with bonded FRP jackets or post-tensioned FRP shells. In: Proceedings of the 8th International Symposium on Fiber Reinforced Polymer Reinforcement for Concrete Structures. Patras: University of Patras, 2007
30. Binici B. Design of FRPs in circular bridge column retrofits for ductility enhancement. Engineering Structures, 2008, 30(3): 766–776
31. Benzaid R, Mesbah H. FRP-confined concrete cylinders: Axial compression experiments and strength model. Journal of Reinforced Plastics and Composites, 2010, 29(16): 2469–2488
32. Pham T M, Hadi M N, Youssef J. Optimized FRP wrapping schemes for circular concrete columns under axial compression. Journal of Composites for Construction, 2015, 19(6): 04015015
33. Yang J, Wang J, Wang Z. Axial compressive behavior of partially CFRP confined seawater sea-sand concrete in circular columns—Part I: Experimental study. Composite Structures, 2020, 246: 112373
34. Barros J A, Ferreira D R. Assessing the efficiency of CFRP discrete confinement systems for concrete cylinders. Journal of Composites for Construction, 2008, 12(2): 134–148
35. Wang J W. Test study on mechanical performance of C50 concrete cylindrical confined by CFRP under axial load. Thesis for the Master's Degree. Yanji: Yanbian University, 2010 (in Chinese)
36. Campione G, la Mendola L, Monaco A, Valenza A, Fiore V. Behavior in compression of concrete cylinders externally wrapped with basalt fibers. Composites. Part B, Engineering, 2015, 69: 576–586
37. Chen W P. Experimental study on confined concrete with CFRP strip. Thesis for the Master's Degree. Guangzhou: Guangdong University of Technology, 2017 (in Chinese)
38. Wang W, Sheikh M N, Al-Baali A Q, Hadi M N. Compressive behaviour of partially FRP confined concrete: Experimental observations and assessment of the stress–strain models. Construction and Building Materials, 2018, 192: 785–797
39. Duan Z J. Experimental and confinement mechanism research of FRP strips confined concrete. Thesis for the Master's Degree. Guangzhou: Guangdong University of Technology, 2020 (in Chinese)
40. Zhang R. Axial compressive behavior of CFRP-confined lightweight aggregate concrete reinforced with hybrid fibers. Thesis for the Master's Degree. Xi'an: Chang'an University, 2021 (in Chinese)
41. Han T, Dong Z, Zhu H, Wu G, Zhao X. Compression behavior of concrete columns combinedly confined by FRP externally wrapped Fe-SMA strips. Engineering Structures, 2023, 294: 116754
42. Zhang L K. Analysis of mechanical properties of concrete columns with circular section confined by CFRP. Jinan: Shandong University, 2023 (in Chinese)
43. Li W, Li W, Lu Y, Hu B, Zhou Y, Wu H, Wang P, Ke L, Yu J. Axial compressive behavior and failure mechanism of CFRP partially confined ultra-high-performance concrete (UHPC). Construction and Building Materials, 2024, 426: 136104
44. Zou Y. Evaluation of the strain response of FRP partially confined concrete using FEM and DIC testing. International Journal of Structural Integrity, 2024, 15(2): 262–282
45. Shayanfar J, Barros J A, Rezazadeh M. Unified model for fully and partially FRP confined circular and square concrete columns subjected to axial compression. Engineering Structures, 2022, 251: 113355